Received: 19 December 2023 | Revised: 26 February 2024 | Accepted: 21 March 2024

DOI: 10.1002/mrm.30108

RESEARCH ARTICLE

Magnetic Resonance in Medicine

Performance of receive head arrays versus ultimate intrinsic SNR at 7 T and 10.5 T

Bei Zhang[1] | **Jerahmie Radder**[2] | **Ilias Giannakopoulos**[3] | **Andrea Grant**[2] | **Russell Lagore**[2] | **Matt Waks**[2] | **Nader Tavaf**[2] | **Pierre-Francois Van de Moortele**[2] | **Gregor Adriany**[2] | **Alireza Sadeghi-Tarakameh**[2] | **Yigitcan Eryaman**[2] | **Riccardo Lattanzi**[3] | **Kamil Uğurbil**[2]

[1]Advanced Imaging Research Center, UT Southwestern Medical Center, Dallas, Texas, USA

[2]Center for Magnetic Resonance Research (CMRR), University of Minnesota, Minneapolis, Minnesota, USA

[3]Center for Advanced Imaging Innovation and Research (CAI^{2}R) and Bernard and Irene Schwartz Center for Biomedical Imaging, Department of Radiology, New York University Grossman School of Medicine, New York, New York, USA

Correspondence

Bei Zhang, Advanced Imaging Research Center, UTSW, 2201 Inwood Rd, Dallas, TX 75390, USA.

Email: bei.zhang2@utsouthwestern.edu

Funding information

Cancer Prevention and Research Institute of Texas, Grant/Award Number: RR180056; National Institutes of Health, Grant/Award Numbers: NIH U01 EB025144, NIH P41 EB017183, NIH R01 EB024536, NIH P41 EB027061

Abstract

Purpose: We examined magnetic field dependent SNR gains and ability to capture them with multichannel receive arrays for human head imaging in going from 7 T, the most commonly used ultrahigh magnetic field (UHF) platform at the present, to 10.5 T, which represents the emerging new frontier of >10 T in UHFs.

Methods: Electromagnetic (EM) models of 31-channel and 63-channel multichannel arrays built for 10.5 T were developed for 10.5 T and 7 T simulations. A 7 T version of the 63-channel array with an identical coil layout was also built. Array performance was evaluated in the EM model using a phantom mimicking the size and electrical properties of the human head and a digital human head model. Experimental data was obtained at 7 T and 10.5 T with the 63-channel array. Ultimate intrinsic SNR (uiSNR) was calculated for the two field strengths using a voxelized cloud of dipoles enclosing the phantom or the digital human head model as a reference to assess the performance of the two arrays and field depended SNR gains.

Results: uiSNR calculations in both the phantom and the digital human head model demonstrated SNR gains at 10.5 T relative to 7 T of 2.6 centrally, ~2 at the location corresponding to the edge of the brain, ~1.4 at the periphery. The EM models demonstrated that, centrally, both arrays captured ~90% of the uiSNR at 7 T, but only ~65% at 10.5 T, leading only to ~2-fold gain in array SNR in going from 7 to 10.5 T. This trend was also observed experimentally with the 63-channel array capturing a larger fraction of the uiSNR at 7 T compared to 10.5 T, although the percentage of uiSNR captured were slightly lower at both field strengths compared to EM simulation results.

Conclusions: Major uiSNR gains are predicted for human head imaging in going from 7 T to 10.5 T, ranging from ~2-fold at locations corresponding to the edge of the brain to 2.6-fold at the center, corresponding to approximately quadratic increase with the magnetic field. Realistic 31- and 63-channel receive

---

This is an open access article under the terms of the Creative Commons Attribution-NonCommercial-NoDerivs License, which permits use and distribution in any medium, provided the original work is properly cited, the use is non-commercial and no modifications or adaptations are made.
© 2024 The Authors. *Magnetic Resonance in Medicine* published by Wiley Periodicals LLC on behalf of International Society for Magnetic Resonance in Medicine.

arrays, however, approach the central uiSNR at 7 T, but fail to do so at 10.5 T, suggesting that more coils and/or different type of coils will be needed at 10.5 T and higher magnetic fields.

KEYWORDS

electromagnetic models, multichannel receive array, ultrahigh field MRI, ultimate intrinsic signal-to-noise ratio

1 | INTRODUCTION

Magnetic field dependent increases in ultimate intrinsic SNR (uiSNR),[1–6] the theoretical upper-bound of achievable SNR, are central to efforts aimed at exploiting ultrahigh magnetic fields for MR based biomedical research, particularly those targeting the human brain.[7–15] Capturing this uiSNR advantage requires RF coil arrays composed of distributed receive elements.[16] Using electromagnetic (EM) field simulations, the number of elements required to maximize the SNR in a sphere with dimensions and electrical properties approximating the human head was shown to depend on the magnetic field strength and spatial location[17]; 32 loop elements were sufficient for capturing most of the uiSNR in the central regions at the magnetic fields examined while at the periphery, where uiSNR is intrinsically high, a larger number of elements continued to provide increasing gains. However, these conclusions are based on analytical EM models of idealized conditions. Although extremely useful in providing insights, such studies do not fully capture the complexities involved in realistic experimental conditions. RF coils used for imaging the human brain cannot fully enclose the human head and individual coil elements of the array can deviate from the conventional loop design, particularly at ultrahigh fields (UHF, defined as ≥7 T). For example, although the idealized loop in the analytical simulations is a perfect circle with uniform current distribution, a conventional loop coil can be transformed into a loopole[18] or self-decoupled loop[19,20] by changing the distribution of capacitors on the coil conductor,[18,19] therefore, significantly altering its current distribution, affecting its sensitivity, and impacting the interaction among coil elements in the array. Similarly, other RF coil types, such as dipoles[21,22] and striplines,[23] which become usable at UHFs, can impact the spatial distribution of the experimental SNR attainable in a given array configuration. Therefore, relying solely on analytical simulations of idealized coil geometries is inadequate to accurately evaluate dense array designs. Instead, realistic EM models of dense array prototypes are required to validate and refine the results. Although such realistic simulations can be time consuming because of the need for fine meshing in the case of dense arrays, and they may fail to fully capture the experimental conditions, for example, with respect to the noise contribution, they are nevertheless crucial because of the limited availability of dense array designs to reference at UHFs. This is particularly relevant for the emerging field of >10 T MR,[24–30] where experience is scarce in designing and building such arrays. Alternative approach of relying only on experimental evaluations of possible array configurations across magnetic fields for different numbers of coil elements and types would be a daunting and expensive task.

The maximum achievable SNR for a given imaging sample irrespective of the coil geometry is the uiSNR,[1] and it serves as an absolute reference for evaluating coil array performance. Initially, uiSNR was calculated in simple geometries. For instance, Lattanzi and Sodickson[31] proposed a dyadic Green's functions (DGF) simulation framework for uiSNR calculation in homogeneous anatomy-mimicking spheres and cylinders. Recent developments in volume integral equation methods have extended the uiSNR calculation to realistic and non-uniform body models.[3,32] This approach enables the assessment of the absolute performance of a head array with heterogeneous numerical head models or phantoms of arbitrary shape.

In this study, we simulated 31- and 63-channel array prototypes at 7 T and 10.5 T. The array SNR from EM modeling and experimental measurements were evaluated in the context of uiSNR calculated at 7 T and 10.5 T for a head shape phantom and the realistic Duke model from the virtual family.[33] To our knowledge, this is the first article that combines detailed EM modeling of actual coils built, uiSNR calculations, and corresponding experimental data to evaluate performance in both simulations and matched experiments. This approach and its applications to a >10 T field strength for the first time provides new insights into this new >10 T territory, with novel conclusions about the ability to capture uiSNR and achievable field dependent SNR gains in multichannel receiver arrays. The results demonstrate that generalizations that emerged based on previous work are not necessarily applicable for the emerging field of imaging at magnetic fields greater than 10 T.

15222594, 2024, 3, Downloaded from https://onlinelibrary.wiley.com/doi/10.1002/mrm.30108, Wiley Online Library on [01/08/2024]. See the Terms and Conditions (https://onlinelibrary.wiley.com/terms-and-conditions) on Wiley Online Library for rules of use; OA articles are governed by the applicable Creative Commons License

2 | METHODS

The simulations and the experiments used a phantom that was shaped like a "light bulb" with the larger section mimicking approximately the human head dimensions, and the narrower end simulating the neck. The phantom was filled with polyvinylpyrrolidone (PVP) gel that had electrical properties of $\varepsilon_r = 47.25$ and $\sigma = 0.646$ S/m at 447 MHz (^{1}H frequency at 10.5 T) and $\varepsilon_r = 49.56$ and $\sigma = 0.561$ S/m at 297.2 MHz (^{1}H frequency at 7 T). This phantom is routinely used for experimental measurements for characterizing coils in the Center for Magnetic Resonance Research (CMRR) at the University of Minnesota. The 10.5 T scanner in CMRR represents the first effort at human imaging at >10 T and, as such, operates under an investigational device exemption (IDE) from the United States Food and Drug Administration. This IDE requires that each RF coil is United States Food and Drug Administration -approved before use in humans. A critical step in this approval is the validation of the EM models developed for the arrays; however, such data cannot be obtained in the human head and must rely on phantoms mimicking the human head in shape and average electrical properties. Therefore, the selected phantom is used for this purpose and provides a common platform for both simulation and the experimental data needed in the coil evaluation and development phase.

The EM simulations were based on two real arrays developed at 10.5 T. The built prototypes were originally configured as 32- and 64-channel receive arrays. However, one element that was at the very top of the head and oriented with the plane of the loop perpendicular to the z-axis did not contribute much to SNR and was disabled. As such the built prototypes became 31 and 63 receive arrays and were modeled as such. The arrays were retuned and rematched in the EM model to generate the corresponding arrays tuned for 7 T. The experimental set up was accurately simulated using a 3D computer aided design software, SolidWorks (Dassault Systems). The modeling included various components such as a head-conformal close-fitting coil holder, coil layout, RF shield, and the lightbulb-shaped phantom. An identical 63-channel array was also built for 7 T, but not for the 31 channel array for direct experimental comparisons.

The EM model of the 31- and 63-channel array prototypes are presented in Figure 1. The bottom row in this figure (Figure 1D) also shows pictures (a front and a back view) of the built 63-channel receive array prototype. The 31-channel array was built identically to what is shown in Figure 1D, except the loop sizes and the numbers were different. The design of the coil holder in the EM model closely mimicked the experimental setup, featuring XY-plane traces that allowed for the placement of copper wires for the coil elements. The 31- and 63-channel arrays were composed of four and six rows of coil elements along the z-direction, respectively (Figure 1B).

The view of the model presented in Figure 1B illustrates that the first row of coil elements in the 31-channel array only contained three coil elements in the brain stem area and did not provide coverage azimuthally. The remaining three rows of coil elements fully circumscribed the former. Azimuthally, the second row contained 10 coil elements, the third row 12 coil elements, and the fourth row six coil elements. In the 63-channel array, the location of the first and second rows of coil elements overlapped with the opening in the front of the coil. The distribution of coil elements in this array was as follows: six coil elements in the first row, 11 in the second row, 14 in the third row, 16 in the fourth row, eight in the fifth row, and an additional eight in the sixth row. In both the 31- and 63-channel arrays, the coil elements within different rows along the z-direction were overlapped. To achieve decoupling, intentional gaps were introduced between the coil elements within the same row following the self-decoupled loop technology proposed by Yan et al.[18]

The coil elements were modeled using 1-mm-diameter spline, identical in diameter to the copper wire used in the prototypes that were built. To prevent electrical connection in overlapping areas of the coil elements, arc-shaped jumps were used at the same locations as the prototype. Additionally, each coil element was segmented to include tuning capacitors and feeding ports at the same locations as in the coil prototype. The modeling also included a 640-mm-diameter gradient shield in the scanner.

The 3D CAD model of the experimental setup was imported into CST Microwave Studio (Dassault Systems), a commercial software based on the finite integration technique for EM simulation. Fixed capacitors were placed on the segments of each coil element with the same capacitance as used in the actual prototype, and a resistance of 0.1 Ω was added to each fixed capacitor to emulate the equivalent series resistance of the capacitors. Two 50-Ω ports were placed on each coil element, one at the variable tuning capacitor location and the other at the port. Therefore, a total of 62 ports were run for the 31-channel array and 126 ports for the 63-channel array in the CST time-domain solver. The modeled coils were numbered in the same order as the grouping of the coil elements in the 31- and 63-channel array prototypes, respectively. To ensure convergence and avoid truncation error in the Fourier transformation, a relative attenuation threshold of 40 dB was set for the amplitude of the signal at the input ports at the end of simulation time interval for all simulations. An absorbing boundary condition was set at the edge of the gradient shield to minimize the reflected power.

15222594, 2024, 3, Downloaded from https://onlinelibrary.wiley.com/doi/10.1002/mrm.30108, Wiley Online Library on [01/08/2024]. See the Terms and Conditions (https://onlinelibrary.wiley.com/terms-and-conditions) on Wiley Online Library for rules of use; OA articles are governed by the applicable Creative Commons License

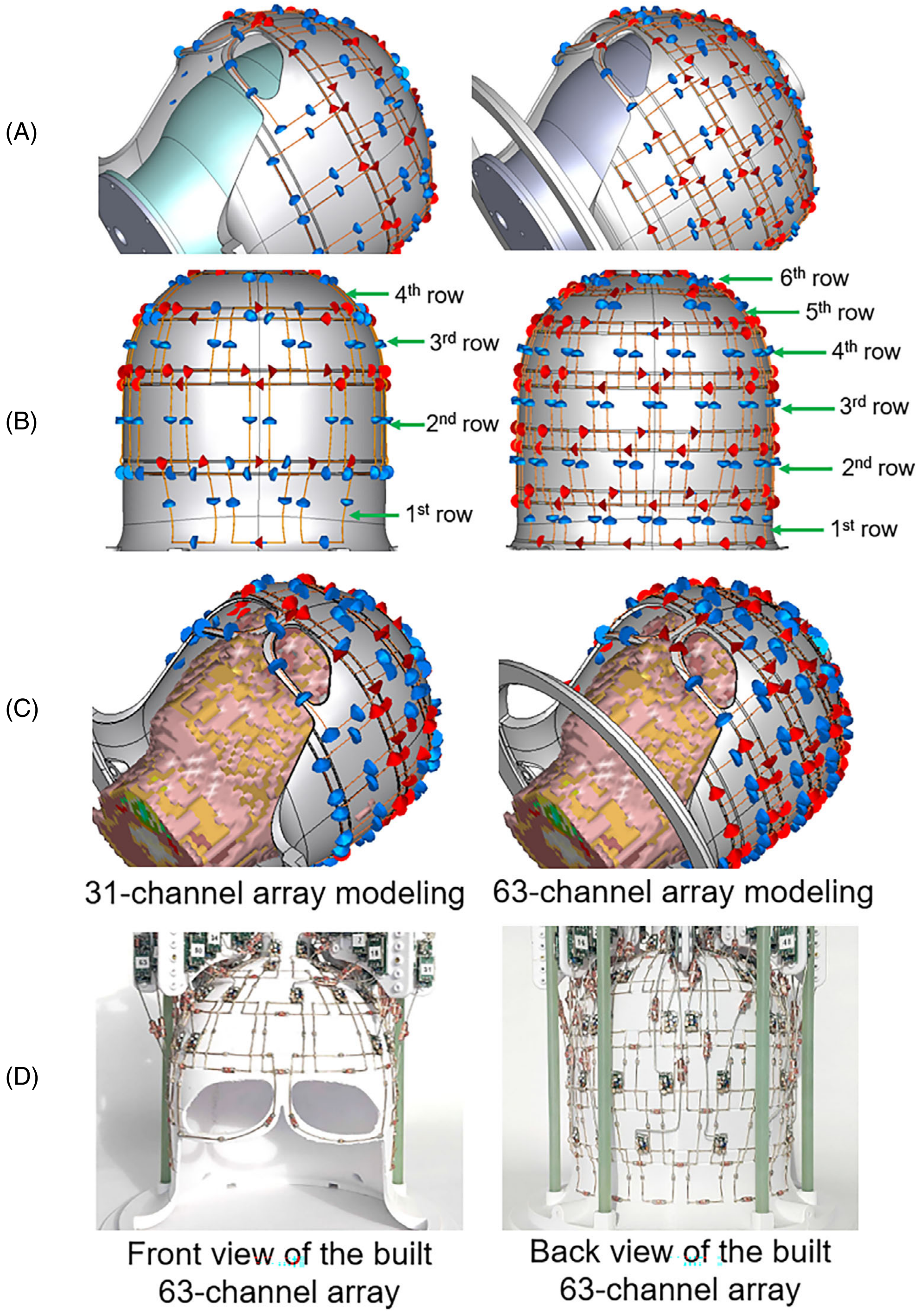

FIGURE 1 (A) Side view of electromagnetic modeling of the 31-channel and 63-channel arrays with the light bulb phantom; (B) back view of electromagnetic modeling of the 31-channel and 63-channel arrays with the light bulb phantom; (C) side view of electromagnetic modeling of the 31-channel and 63-channel arrays with the Duke head model, and all models were developed in CST Microwave Studio; and (D) front view and back view of the built 63-channel array prototypes.

For the existing 10.5 T 31- and 63-channel array prototypes, we also performed simulations loading them with the 5 mm × 5 mm × 5 mm Duke model[33] to estimate the coil performance in the in vivo scans. The Duke model was truncated to include only the head and neck, as shown in Figure 1C, to shorten the simulation duration.

The tuning and matching of each coil element were achieved using the circuit simulator in CST. To replicate the preamplifier decoupling effect, a high impedance of 2500 Ω was introduced at the ports of all other coil elements while tuning and matching an individual coil. This iterative process was repeated twice to ensure that all the coil elements were tuned and matched at the operating frequency. Subsequently, the electric and magnetic fields of each coil element were reconstructed and exported from CST with a resolution of 5 mm × 5 mm × 5 mm. The intrinsic noise correlation matrix was calculated using the electric fields, whereas the receive coil sensitivities were determined using the magnetic fields. Finally, an optimal coil combination[34,35] was calculated to estimate the SNR at

15222594, 2024, 3, Downloaded from https://onlinelibrary.wiley.com/doi/10.1002/mrm.30108, Wiley Online Library on [01/08/2024]. See the Terms and Conditions (https://onlinelibrary.wiley.com/terms-and-conditions) on Wiley Online Library for rules of use; OA articles are governed by the applicable Creative Commons License

each voxel. Maps of the inverse g-factor[36] were calculated by decimating fully sampled data of the simulated SNR for various acceleration factors using in-house software.[37]

The uiSNR[1–6] was calculated as a reference to assess the two arrays at both 7 T and 10.5 T. To calculate the uiSNR inside the light bulb phantom and the head model, we enclosed each object with a voxelized cloud of dipoles (1.5 cm thickness and 4 cm minimum distance from the sample).[38] The dipole cloud and the samples were discretized on uniform grids using piecewise constant basis functions[39] and 5-mm isotropic voxel resolution. A numerical basis of excitation EM fields was then generated for each sample at each field strength using a randomized singular value decomposition (RSVD) approach as in Giannakopoulos et al.[32] We stopped the RSVD when the singular values dropped to 10^{-5}, which resulted in ∼500 basis vectors for all cases. The corresponding EM fields were derived following the methods in Polimeridis et al.[40] and used to compute the uiSNR as in Lattanzi et al.[41] The sample electrical properties were adjusted based on the field strength. The absolute performance of the arrays was calculated as the ratio of their SNR to the corresponding uiSNR.[3] All uiSNR computations were performed in MATLAB 9.10 (The MathWorks) on a server running Ubuntu 18.04.2 LTS operating system, with an Intel(R) Xeon(R) Gold 6248R CPU at 2.70 GHz, 112 cores, two threads per core, and an NVIDIA A100 PCIe GPU with 40 GB of memory.

For experimental measurements, each receive array was inserted in a separate circumscribing 16-channel transmitter. The elements of the transmit array were laid out in a dual row arrangement along the z-direction and mounted on a 28.5 cm ID cylindrical former. Each of the two rows contained eight self-decoupled[18] square loops measuring 10×10 cm^2. The two rows were offset from one another, with the inferior row having a 22.5° azimuthal rotation (around the z-axis) compared to the superior row. There was a gap of 1 cm between neighboring loops as well as the two different rows (along the z-axis). This coil arrangement replicates our previous 10.5 T transformer-decoupled transmit array.[42] The coil former was designed and 3D printed (Fusion3 F410) in-house using PETG filament. All feed circuits were equipped with coaxial cable traps[43]; these cable traps attenuate common-mode currents and reduce induced currents from the transmitter elements. The array circuit artwork was fabricated (PCBWay) with 35-μm copper conductors etched onto a flexible polyimide substrate. Individual coil tuning and matching was achieved with both fixed (KYOCERA AVX) and variable (Sprague Goodman) capacitors. This transmitter was described previously.[44] Another version of the same transmitter with identical layout, but modified with transmit/receive switches and on-board preamplifiers so as to convert it to a transmit/receive array was also previously described.[45] An unpopulated model of this transmit array (i.e., without capacitors and any other lumped circuit elements) was included in all the EM simulations to account for the shielding effect of the transmit coil conductors on the receive array performance. Although a description of the transmitter used is presented above, all SNR measurements were normalized by the flip angle so as to be independent of the transmitter performance.

All experimental SNR measurements were performed with the aforementioned PVP-gel filled uniform lightbulb-shaped phantom. SNR data was reconstructed from fully sampled 2D-gradient echo sequences with a long TR for full relaxation (TR = 10 000 ms, TE = 3.48 ms, full bandwidth = 87 kHz, voxel size = $2.0 \times 1.0 \times 2.0$ mm^3). Noise images were acquired with identical parameters, but without RF excitation and TR of 600 ms. To compare the measured SNR with the uiSNR, the former was scaled by the experiment-related parameters as described in Lattanzi et al.[46] and Gruber et al.[47]:

$$\zeta_{\text{Scaled}}(\overline{r}) = \zeta_{\text{Measured}}(\overline{r}) \times \frac{F\sqrt{\Delta f}}{V_{\text{voxel}}\sqrt{N_{\text{acq}} NEX}\,\sin(\alpha(\overline{r}))} \times \frac{1}{\rho e^{-TE/T_{2^*}}}$$

where $\zeta(\overline{r})$ is the SNR at location r, F is the noise factor of the system (assumed to be 1.15 based on manufacturer specifications), Δf is the receiver bandwidth, V_{voxel} is the volume of the voxel, N_{acq} is number of the acquired k-space samples, NEX is the number of averaging, $\alpha\left(\overline{r}\right)$ is the measured flip angle at location r, ρ is the proton density of the PVP phantom (measured as 0.69), and TE is the echo time. The T_2* of the phantom measured as 24 ms at 10.5 T and linearly extrapolated to 36 ms at 7 T, which was confirmed experimentally to be correct. The T_2* values were lower at the periphery of the phantom, particularly for 10.5 T, as expected from the field inhomogeneities at the air-phantom interface, but were spatially uniform for the reported values within a large volume centrally where SNR comparisons were made.

3 | RESULTS

Figure 2 displays the simulated intrinsic noise correlation matrix for the two arrays at 7 T and 10.5 T. The 31-channel array (Figure 2, left column) shows small off-diagonal values at 10.5 T because the coil elements of this array are self-decoupled at this field strength. In contrast, the coil elements in the 7 T 31-channel array have higher coupling likely because the coil elements deviate from being

15222594, 2024, 3, Downloaded from https://onlinelibrary.wiley.com/doi/10.1002/mrm.30108, Wiley Online Library on [01/08/2024]. See the Terms and Conditions (https://onlinelibrary.wiley.com/terms-and-conditions) on Wiley Online Library for rules of use; OA articles are governed by the applicable Creative Commons License

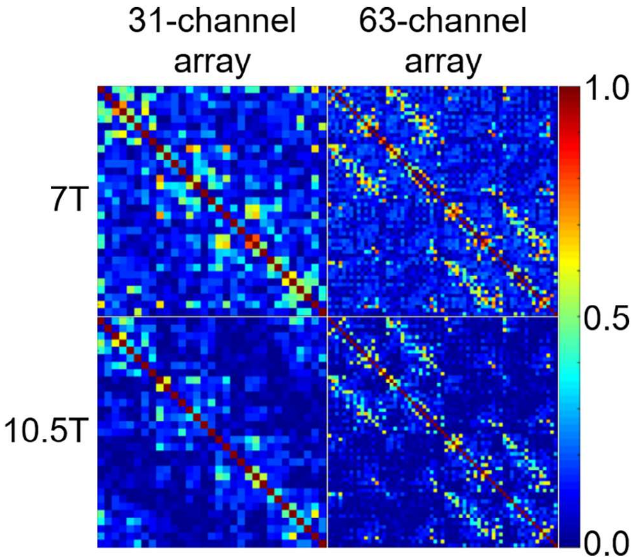

FIGURE 2 Noise correlation matrixes calculated from the simulated electric fields for the 31-channel and 63-channel arrays loaded with the light bulb phantom at 7 T (top) and 10.5 T (bottom).

self-decoupled at the lower frequency for this coil size. In addition, because the electric fields inside the sample decays faster at higher frequency and start canceling out because of wave behavior,[48] the coils at 10.5 T experience/share lower sample noise compared to the coils of the same size at 7 T. The coil elements of the 63-channel arrays deviate from the self-decoupling condition because of their small size both at 7 and 10.5 T; as such, their noise correlation matrices are similar (Figure 2, right column).

Parallel imaging performance of the two arrays at the two field strengths were examined from the EM modeling. For this purpose, inverse g-factor maps for the 31-channel and 63-channel arrays at both 7 T and 10.5 T, for various acceleration factors (1 × 2, 2 × 2, 3 × 3, and 4 × 4) were computed and presented in Figure 3. Both arrays demonstrated enhanced acceleration performance at 10.5 T when compared to 7 T. Moreover, the 63-channel array showed superior acceleration performance as compared to the 31-channel array both at 7 T and 10.5 T.

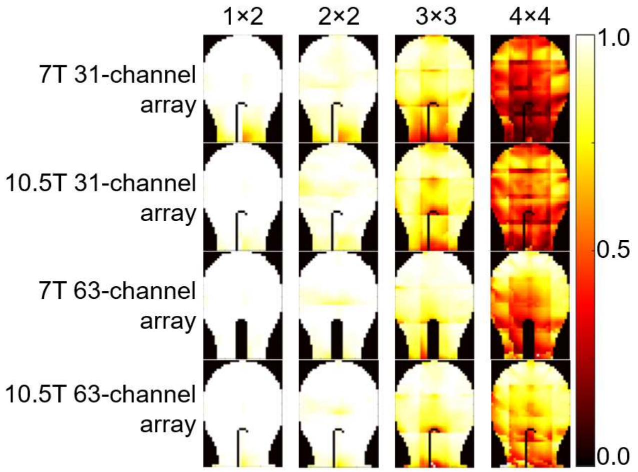

FIGURE 3 Inverse g-factor maps of 31-channel array and the 63-channel array for various acceleration factors at 7 T and 10.5 T, for a sagittal plane through the center for the light bulb phantom.

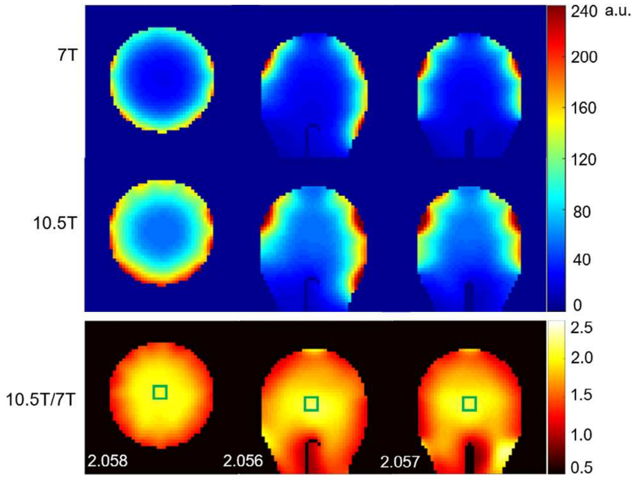

FIGURE 4 SNR maps calculated from the electromagnetic simulations for the 7 T 31-channel array (top row), 10.5 T 31-channel array (middle row), and the corresponding 10.5 T to 7 T SNR ratio maps (bottom row) for three orthogonal sections through the center of the light bulb phantom. The numbers in the left corner of the bottom row correspond to the average SNR ratio value in the central 5 × 5 × 5 mm voxel region of interest depicted in green bottom row).

Figures 4 and 5 compare the intrinsic SNR maps at 7 T and 10.5 T for the 31-channel and 63-channel arrays, respectively. These maps show a ~2-fold SNR increase at 10.5 T relative to 7 T in the center (within a 5 mm isotropic voxel) and between 1.35+/0.08-fold increase in the outer region in transversal plane for the 31-channel array, where the outer region was defined as the entire area subtracted a 150-mm-diameter circle from the center. For the 63-channel array, the SNR gain in the center at 10.5 T relative to 7 T was ~2.10, slightly larger compared to the 31-channel array, whereas the average field-dependent increase in the periphery was comparable with the 31-channel array. For both arrays at both field strengths, the SNR was considerably larger at the periphery compared to the center, but the 63-channel array prototype exhibited a larger volume of higher SNR in going from the center toward the periphery compared to the 31-channel array at both field strengths. In addition, 10.5 T also displayed a larger volume of higher SNR near the periphery compared to 7 T.

Figure 6 presents that SNR data as a ratio of 63- versus 31-channel arrays; near the surface of the phantom, the SNR of the 63-channel array was considerably higher than the SNR of the 31-channel array at both 7 T and 10.5 T as expected.[46] The central SNR on the other hand

15222594, 2024, 3, Downloaded from https://onlinelibrary.wiley.com/doi/10.1002/mrm.30108, Wiley Online Library on [01/08/2024]. See the Terms and Conditions (https://onlinelibrary.wiley.com/terms-and-conditions) on Wiley Online Library for rules of use; OA articles are governed by the applicable Creative Commons License

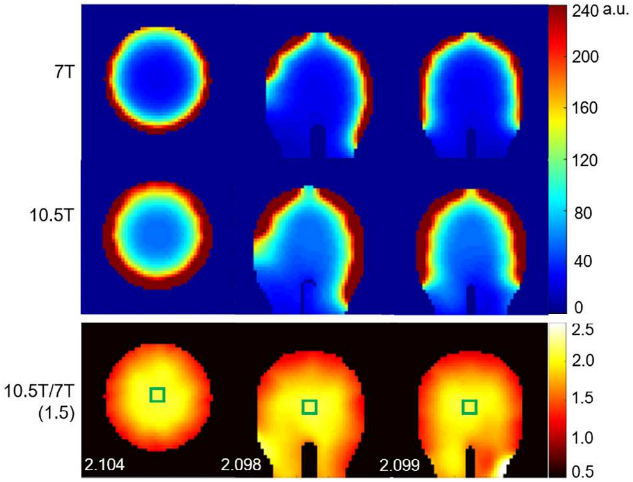

FIGURE 5 SNR maps of the 7 T 63-channel array (top row), 10.5 T 63-channel array (middle row), and the corresponding 10.5 T to 7 T SNR ratio maps (bottom row) for three orthogonal slices through the center of the light bulb phantom. The numbers in the lower left corner of the three panels in the bottom row report the average SNR ratio value in the central 5 × 5 voxel region of interest depicted in green (bottom row).

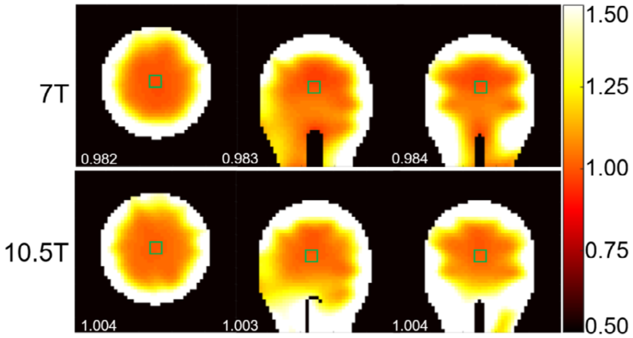

FIGURE 6 SNR ratio maps of the 63-channel array relative to the 31-channel array at 7 T (top) and 10.5 T (bottom). The numbers in the lower left corners correspond to the average value in the $5 \times 5 \times 5\ \text{mm}^3$ voxel region of interest depicted in green.

was comparable for the two arrays both at 7 T and 10.5 T, although a marginally lower SNR for the 63- compared to the 31-channel array was noted centrally at 7 T.

Figure 7 shows the ratio of uiSNR at 10.5 T compared to that at 7 T ($\text{uiSNR}_{10.5\text{T}/7\text{T}}$) for the light bulb phantom and the numerical head model. The overall $\text{uiSNR}_{10.5\text{T}/7\text{T}}$ patterns in the human head and the phantom were very similar. For both samples, when the field strength increased from 7 T to 10.5 T, the uiSNR increased by ~1.4-fold in the periphery, ~2-fold at the edge of the brain as determined from the head model, and ~2.6-fold in the central region as measure within the 5-mm isotropic ROI.

Figure 8 shows the coil performance maps presented as percentage of simulated array SNR to uiSNR ratio ($\text{SNR}_{\text{array}}$/uiSNR) for both arrays at 7 T and 10.5 T, for

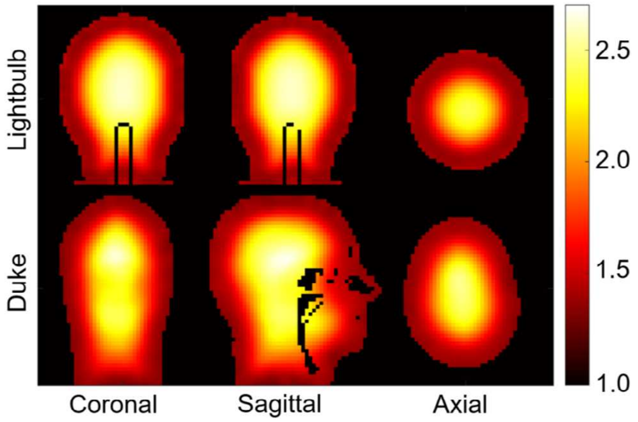

FIGURE 7 Ultimate intrinsic SNR (uiSNR) as a ratio of 10.5 T to 7 T (uiSNR10.5 T/7 T) displayed as maps in three orthogonal planes (sagittal, coronal and axial, respectively from left to right) through the center of the light bulb phantom (top) and the Duke human head model (bottom). The values in all maps are comparable, showing a ~2.6-fold increase in performance in the central region and ~1.4-fold increase near the surface.

the light bulb phantom. The mean and maximum performance values throughout the entire volume of the sample are shown at the bottom of each sub-figure. The $\text{SNR}_{\text{array}}$/uiSNR ratio measured from the EM simulation data (Figure 8) was compared to experimentally measured $\text{SNR}_{\text{array}}$/uiSNR ratio for a centrally located 2-cm diameter sphere (Figure 9). The EM modeling data illustrate that at 7 T, both arrays can achieve ~90% of the uiSNR in this central volume of interest in the light bulb phantom, indicating that both designs are close to being optimal centrally. However, at 10.5 T, the same arrays can achieve only ~65% uiSNR in the same volume of interest. A similar trend was observed with the experimentally determined array SNR relative to uiSNR for the same light bulb phantom and over the same volume of interest (centrally located sphere of 2-cm diameter); this was obtained using a 7 T array that was built with the identical coil layout as the 10.5 T 63-channel, as described in Methods. The experimental $\text{SNR}_{\text{array}}$/uiSNR ratio for the 63-channel arrays was measured centrally in the same 2-cm diameter sphere as used for the EM simulations; experimental $\text{SNR}_{\text{array}}$/uiSNR ratio was 76% at 7 T and 58% at 10.5 T. The $\text{SNR}_{\text{array}}$/uiSNR ratio maps in Figure 9A demonstrate the absolute coil performance is low at 10.5 T relative to 7 T over a much large volume located centrally. Although the $\text{SNR}_{\text{array}}$/uiSNR values at each field strength differ between the simulation and experimental data, they both show the same trend, namely that the identical 63-channel arrays capture less of the uiSNR at 10.5 T than at 7 T.

Figure 10 shows the SNR performance maps for both the 31- and the 63-channel arrays, loaded with the Duke human head model at 10.5 T. As in the case of the light

15222594, 2024, 3, Downloaded from https://onlinelibrary.wiley.com/doi/10.1002/mrm.30108, Wiley Online Library on [01/08/2024]. See the Terms and Conditions (https://onlinelibrary.wiley.com/terms-and-conditions) on Wiley Online Library for rules of use; OA articles are governed by the applicable Creative Commons License

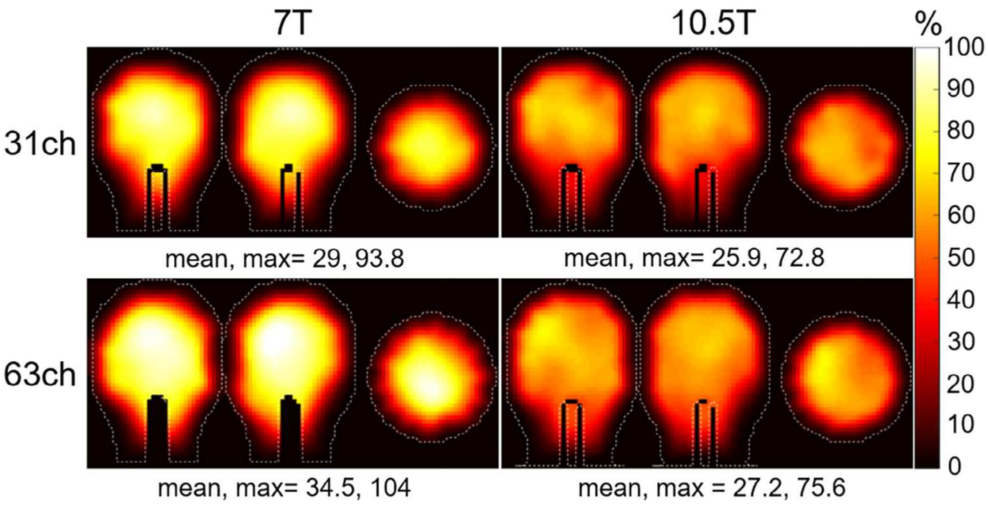

FIGURE 8 Electromagnetic model simulated coil performance as a ratio of the calculated array SNR to ultimate intrinsic SNR (uiSNR) presented as maps for the 31-channel (top) and 63-channel (bottom) arrays loaded with the light bulb phantom at 7 T (left) and 10.5 T (right). The array SNR/uiSNR ratio maps are shown for three orthogonal planes (coronal, sagittal, and axial, respectively from left to right). Note that the maximum performance of the 63-channel array at 7 T is larger than 100% because of the expected ~5% discrepancies between the CST simulations used to calculate the coil SNR and the volume integral equation technique used to calculate the uiSNR.

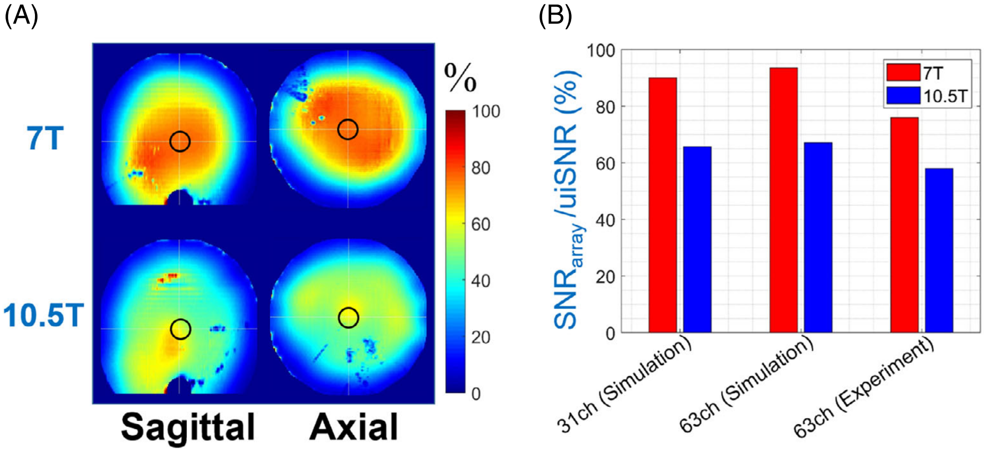

FIGURE 9 Experimental assessment of SNR performance of head arrays relative to ultimate intrinsic SNR (uiSNR) in the “light bulb” phantom (SNRarray/uiSNR). (A) Maps of the experimentally measured SNRarray/uiSNR ratio for the 63-channel head arrays at 7 T and 10.5 T. (B) Central SNR performance of 31-channel (simulation-only) and 63-channel (simulation and experiment) head arrays at 7 T and 10.5 T. The central SNR performance was quantified by averaging the SNRarray/uiSNR ratio within a centrally located sphere of 2-cm diameter depicted in (A).

bulb phantom, neither array could closely approach the uiSNR at 10.5 T, with the 63-channel array having overall the highest performance.

4 | DISCUSSION

UHF of 7 T was developed for increased functional mapping sensitivity (i.e., functional contrast-to-noise ratio [fCNR]) and high spatial resolution imaging of brain activity using FMRI.[11] Much has been accomplished at 7 T in this respect, demonstrating the feasibility of detecting brain activity in mesoscale neuronal organizations in the human brain.[7–9,11,15,47,49–55] However, the need to increase SNR and fCNR further for such studies remains because the current resolutions and the fCNR available at such resolutions are substantially suboptimal. This has been recognized, for example, in the strategic plan for the BRAIN

15222594, 2024, 3, Downloaded from https://onlinelibrary.wiley.com/doi/10.1002/mrm.30108, Wiley Online Library on [01/08/2024]. See the Terms and Conditions (https://onlinelibrary.wiley.com/terms-and-conditions) on Wiley Online Library for rules of use; OA articles are governed by the applicable Creative Commons License

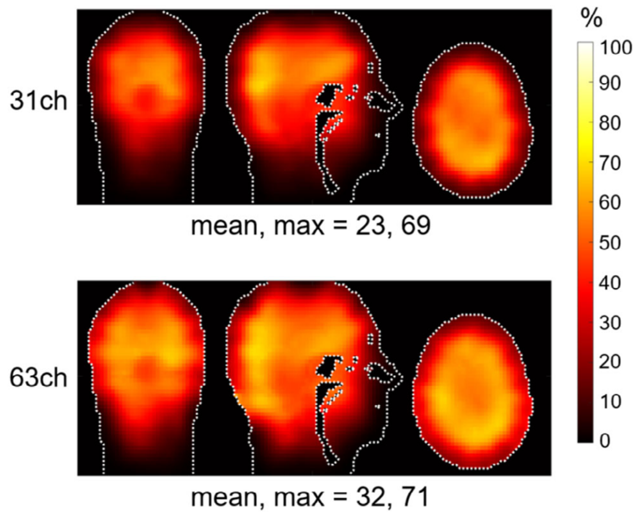

FIGURE 10 Electromagnetic model simulated performance for array SNR versus ultimate intrinsic SNR (uiSNR) ratio (SNR/uiSNR) maps for the 31-channel (top) and 63-channel arrays loaded with the head model at 10.5 T. Mean and maximum performance values throughout the entire volume of the sample are shown at the bottom of each row.

Initiative launched by the National Institutes of Health[56] in the United States, which set challenging resolution targets for FMRI.[57] Efforts to push human MR imaging to fields >10 T are expected to provide at least in part the gains necessary to meet this challenge. A central question of such >10 T efforts is what are the SNR gains that can be realized at such field strengths and how to capture them in the human head. In this article, we tackle this question for 10.5 T, the magnetic field strength used for one of the >10 T projects and to date the only one where human imaging above 10 T has currently been published.[25,27,30,58]

At UHFs, experimentally determining the field dependence of SNR over the object of interest is a difficult task. This is in part due to the strong impact of coil layout on the magnitude and spatial distribution of B_1 fields[59] induced by the traveling wave behavior of high-frequency RF in objects with the size and electrical properties of the human head.[15,59,60] For example, it was recently demonstrated that in the center of a 16.5-cm diameter spherical phantom filled with saline water, the experimentally measured SNR increased approximately quadratically with B_0.[26] However, with the RF coil used, this measurement was only possible and meaningful in the center of the sphere where B_1^+ and B_1^- fields from all current carrying elements add constructively in such a coil, whereas outside this small central region, they add destructively leading to signal cancelation and SNR loss with increasing field strength.[60]

Alternatively, the concept of uiSNR provides a framework for ascertaining the maximal achievable SNR gains as a function of field magnitude irrespective of the specific layout or the performance of RF coils. As such, it also provides a reference against which realistic RF coil designs can be evaluated. Such comparisons are facilitated by the fact that recent developments permit the calculation for uiSNR for more complex phantom shapes than a simple sphere and even in human head models.[3,40]

In this study, we focus on SNR gains at 10.5 T relative to 7 T and the ability of high channel count receive arrays laid out on a former conformal with the human head to capture this SNR increase. Such arrays have been the standard approach used for human head imaging at 7 T and lower magnetic fields. We simulated a 31- and a 63-channel receive array at 7 T and 10.5 T, respectively, based on actual arrays built for 10.5 T.[61,62] The simulated 7 T versions were obtained, as described in the Methods section, by retuning the individual coils to 7 T. A 63-channel array was also built for 7 T for comparisons of experimental and simulation data. The simulation results showed a good match with experimental results in terms of the receive profile and the noise correlation matrix.

The 10.5 T 31-channel array was designed to have self-decoupled coil elements by deliberately selecting the size of each coil element, the number of gaps for fixed tuning capacitors, the capacitance of each fixed tuning capacitor (3.3 pF), and the variable tuning capacitor. In the 7 T 31-channel array, the size of each coil element remained unchanged, and the capacitance of the fixed tuning capacitors was increased to 10 pF. This simple scaling was not sufficient to ensure self-decoupling of the coil elements. Consequently, the off-diagonal elements in the noise correlation matrix of the 7 T 31-channel array were higher compared to the 10.5 T 31-channel array (Figure 2), where the coil element functioned as a loophole because of uneven capacitor distribution on the coil element.[18] Despite this, the similar capacitor distribution on the coil element resulted in a similar uneven current distribution and comparable receive profile hotspots in the peripheral area in the longitudinal direction for both the 7 T 31-channel array and the 10.5 T 31-channel array. The existence of such uneven receive profile was also reported in Lakshmanan et al.[18]

In the case of the 10.5 T and the 7 T 63-channel arrays, the fixed capacitors had identical values as their 31-channel counterparts, but the size of each coil element was significantly smaller. This allowed the capacitance of the variable tuning capacitors to be comparable to that of the fixed capacitor, enabling each coil element to act as a conventional loop. Consequently, both the 7 T and the 10.5 T 63-channel arrays exhibited a uniform receive profile in the peripheral region and a similar coupling pattern among the coil elements, as demonstrated by their noise correlation matrices in Figure 2.

15222594, 2024, 3, Downloaded from https://onlinelibrary.wiley.com/doi/10.1002/mrm.30108, Wiley Online Library on [01/08/2024]. See the Terms and Conditions (https://onlinelibrary.wiley.com/terms-and-conditions) on Wiley Online Library for rules of use; OA articles are governed by the applicable Creative Commons License

The inverse g-factor maps for the 31-channel and 63-channel arrays at 7 T and 10.5 T displayed in Figure 3 demonstrated that the acceleration performance is improved for an array with the same number of coil elements at higher field strength, consistent with the expectation that higher fields promote higher acceleration.[6,63,64] Moreover, the 63-channel array showed superior acceleration performance as compared to the 31-channel array, at both 7 T and 10.5 T, again consistent with previous work demonstrating that higher number of channels lead to higher acceleration at a given field strength.[46,65,66]

EM simulations demonstrated that 31- and 63-loop elements in these arrays could capture most of the uiSNR centrally at 7 T. However, this is not the case at 10.5 T, where both the 31- and the 63-channel arrays fall far short of capturing the central uiSNR. A previous modeling study by Vaidya et al.[17] showed that $\gtrsim$32 receive loops would capture most of the central uiSNR at field strengths 3, 7, and 9.4 T, and by extrapolation of data presented in Figure 2 of this article, also at 10.5 T. However, this prediction is based on simulations of idealized conditions using a sphere and a spherical shell substrate that was completely tiled by idealized loop receivers with evenly distributed currents on the loop. Although there is experimental data (including in this article) confirming this prediction at 3 T and 7 T[46,65] no previous experimental data exists at fields greater than 7 T. Therefore, the specific conclusions of the Vaidya et al.[17] article need to be modified to state that in realistic head receive arrays composed of loops, 32 and even 64 elements are insufficient to capture central uiSNR at field >10 T, whereas they do capture it at 7 T (and likely at lower magnetic fields). This conclusion was experimentally confirmed for the 63-channel array (Figure 9) and is also aligned with another numerical simulation study[31] where it was demonstrated that the central SNR performance of a 64-channel loop receiver drops to 80% at 11 T, whereas it is nearly 100% at 7 T (see figure 3 in Lattanzi and Sodickson).[31]

This conclusion is also reflected in the 10.5 T to 7 T SNR ratios obtained from the EM simulations, where both the 63- and 31-channel arrays exhibited only a 2-fold central SNR gain (Figures 4 and 5) compared to the 2.6-fold increase at 10.5 T relative to 7 T predicted by the uiSNR calculations (Figure 7).

The experimental data and the EM simulation for the 63-channel arrays showed the same trends with respect to field dependence of $\mathrm{SNR_{array}}$/uiSNR ratio; however, the experimental $\mathrm{SNR_{array}}$/uiSNR ratio was lower than the corresponding EM simulation values for both 7 T and 10.5 T. The likely cause of this discrepancy is the fact that the noise model used in the EM simulations is significantly simplified compared to real-world scenarios. The meshing of the coil element, for instance, does not accurately capture conductive losses. Additionally, losses from soldering, lumped elements, matching circuit, cable connections between coil elements and preamps, as well as preamp losses are not taken into account in numerical simulations. Nevertheless, the agreement between the experimental and EM simulation data is quite excellent. In particular, both demonstrate that these arrays are capable of capturing a larger fraction of the uiSNR at the lower field compared to the higher field of 10.5 T. As such, they offer valuable insights into practical coil design and suggest that a higher number of channels and/or a different coil layout, and/or incorporating different coil types (e.g., dipoles)[67,68] are necessary to capture the central SNR at this field strength. Preliminary data so far reported as abstracts demonstrated that using 16 bigger loops in addition to the 63-channel of the receive array to make a 80 channel array[45] or replacing seven channels of a 32Rx array with dipoles[68] significantly improved the fraction of central uiSNR captured at 10.5 T. Preliminary experimental data at 10.5 T, reported currently as an abstract,[69] also demonstrated that using 112 smaller and overlapping loops tiled over the same head-conformal former used in the receiver arrays presented in this article captured most of the central uiSNR. This is consistent with the concept that a sufficient number of small loops could automatically mimic the ideal current patterns, behaving as large, distributed loops to maximize SNR at central voxels while the small localized loops also simultaneously maximize SNR in more superficial voxels.[31]

The uiSNR data indicates that, relative to 7 T, the higher magnetic field of 10.5 T should provide ~1.4-fold gain peripherally, 2-fold gain at the edge of the brain, and a 2.6-fold gain centrally (Figure 7); in the context of a model where SNR $\propto B_0^n$, this would yield an exponent n equal to ~1 to ~1.7 peripherally, and $n = 2.36$ centrally. This central uiSNR gain is in good agreement with previously mentioned results reported in Le Ster et al.[26] for the center of a sphere, where experimental data obtained at field strengths 3, 7, 9.4, 10.5, and 11 T were fitted well with SNR increasing as $\mathrm{B_0^{1.94\pm0.16}}$, whereas uiSNR at those fields strengths for the same sphere was best represented with SNR $\propto \mathrm{B_0^{2.13\pm0.03}}$. The good agreement between the Le Ster et al.[26] study and this work is actually better than these numbers suggest. In the Le Ster et al.,[26] the conductivity of the phantom was higher than the average conductivity of the human brain and the phantom employed in this study ($\sigma \sim 1$ S/m[26] vs. ~0.6 S/m). It was, however, also illustrated in Le Ster et al.[26] that SNR would increase with lower conductivity relative to $\sigma \sim 1$ S/m and that this increase would be slightly more for the higher magnetic fields; as such, for the lower conductivity phantom used in this work and for the human head, a somewhat larger SNR increase at 10.5 T relative to 7 T would be predicted compared to what was

15222594, 2024, 3, Downloaded from https://onlinelibrary.wiley.com/doi/10.1002/mrm.30108, Wiley Online Library on [01/08/2024]. See the Terms and Conditions (https://onlinelibrary.wiley.com/terms-and-conditions) on Wiley Online Library for rules of use; OA articles are governed by the applicable Creative Commons License

reported previously in Le Ster et al.[26] This would be consistent with the 2.6-fold increase predicted centrally based on uiSNR calculations in the current work (Figure 7). Such a central SNR gain from 7 T to 10.5 T is not captured with the current arrays. However, as mentioned previously, they have been realized in experiments using larger loops in addition to the small loops of the existing arrays, using smaller loops to generate receive arrays with significantly larger number of channels than 63, or incorporating few dipoles into the receive arrays in addition to the loops (all of which currently reported as abstracts)[45,68,69]; these preliminary observations are consistent with our conclusion that a higher number of channels and/or a different coil layout and/or types are necessary to capture the central uiSNR at 10.5 T and likely at >10 T in general.

The SNR gains predicted for 10.5 T relative to 7 T by uiSNR calculations as well as EM modeling have significant implications for neuroimaging, particularly for BOLD based FMRI; the fCNR, which ultimately determines the achievable resolutions and is an indicator of the sensitivity and robustness of the measurements at any given resolution, is proportional to the product of image SNR and BOLD effect[11] when the noise in the FMRI time series is dominated by thermal noise; this is the case at high resolutions.[70] With the BOLD effect increasing with a liner to quadratic B_0 dependence (according to its vascular origin),[71–73] the product of SNR gains reported here and the BOLD effect predicts approximately square to the fourth power dependence of fCNR on B_0.

5 | CONCLUSION

In this work, we used full-wave simulation to compare the performance of 31- and 63-channel receive head arrays at 7 T and 10.5 T. Experimental data obtained at 7 T and 10.5 T with the 63-channel array is also brought to bear on the inferences derived from the EM modeling. Our results lead to several important conclusions. Realistic 31- and 63-channel receive arrays can capture most of the central uiSNR at 7 T, but fail to do so at 10.5 T. Consequently, these arrays fall short achieving the 2.6-fold SNR gain expected centrally based on uiSNR calculation. These results indicate that that more coils and/or different type of coils will be needed at 10.5 T and higher magnetic fields to fully capture the SNR available in going to the higher magnetic fields. The uiSNR calculations in this study predicted large theoretical SNR gains over the brain, ranging from ∼2-fold at the edge to 2.6-fold centrally, which should provide major gains in neuroimaging in general, and functional brain imaging in particular.

FUNDING INFORMATION

National Institutes of Health, Grant/Award Numbers: NIH U01 EB025144, NIH P41 EB017183, NIH R01 EB024536, NIH P41 EB027061; Cancer Prevention and Research Institute of Texas, Grant/Award Number: RR180056.

ORCID

Bei Zhang https://orcid.org/0000-0002-9718-1594
Ilias Giannakopoulos https://orcid.org/0000-0003-2180-5898
Nader Tavaf https://orcid.org/0000-0002-3002-3794
Pierre-Francois Van de Moortele https://orcid.org/0000-0002-6941-5947
Gregor Adriany https://orcid.org/0000-0002-6428-9005
Alireza Sadeghi-Tarakameh https://orcid.org/0000-0001-5718-6553
Riccardo Lattanzi https://orcid.org/0000-0002-8240-5903

Kamil Uğurbil https://orcid.org/0000-0002-8475-9334

REFERENCES

1. Ocali O, Atalar E. Ultimate intrinsic signal-to-noise ratio in MRI. *Magn Reson Med*. 1998;39:462-473.
2. Wiesinger F, Boesiger P, Pruessmann KP. Electrodynamics and ultimate SNR in parallel MR imaging. *Magn Reson Med*. 2004;52:376-390.
3. Guerin B, Villena JF, Polimeridis AG, et al. The ultimate signal-to-noise ratio in realistic body models. *Magn Reson Med*. 2016;78:1969-1980.
4. Lee HH, Sodickson DK, Lattanzi R. An analytic expression for the ultimate intrinsic SNR in a uniform sphere. *Magn Reson Med*. 2018;80:2256-2266.
5. Schnell W, Renz W, Vester M, Ermert H. Ultimate signal-to-noise- ratio of surface and body antennas for magnetic resonance imaging. *IEEE Trans Antennas Propag*. 2000;48:418-428.
6. Ohliger MA, Grant AK, Sodickson DK. Ultimate intrinsic signal-to-noise ratio for parallel MRI: electromagnetic field considerations. *Magn Reson Med*. 2003;50:1018-1030.
7. De Martino F, Yacoub E, Kemper V, et al. The impact of ultra-high field MRI on cognitive and computational neuroimaging. *Neuroimage*. 2018;168:366-382.
8. Dumoulin SO, Fracasso A, van der Zwaag W, Siero JCW, Petridou N. Ultra-high field MRI: advancing systems neuroscience towards mesoscopic human brain function. *Neuroimage*. 2018;168:345-357.
9. Polimeni JR, Uludag K. Neuroimaging with ultra-high field MRI: present and future. *Neuroimage*. 2018;168:1-6.
10. Yacoub E, Wald LL. Pushing the spatio-temporal limits of MRI and fMRI. *Neuroimage*. 2018;164:1-3.
11. Ugurbil K. Imaging at ultrahigh magnetic fields: history, challenges, and solutions. *Neuroimage*. 2018;168:7-32.
12. De Cocker LJ, Lindenholz A, Zwanenburg JJ, et al. Clinical vascular imaging in the brain at 7T. *Neuroimage*. 2018;168:452-458.
13. Trattnig S, Springer E, Bogner W, et al. Key clinical benefits of neuroimaging at 7T. *Neuroimage*. 2018;168:477-489.

15222594, 2024, 3, Downloaded from https://onlinelibrary.wiley.com/doi/10.1002/mrm.30108, Wiley Online Library on [01/08/2024]. See the Terms and Conditions (https://onlinelibrary.wiley.com/terms-and-conditions) on Wiley Online Library for rules of use; OA articles are governed by the applicable Creative Commons License

14. Obusez EC, Lowe M, Oh SH, et al. 7T MR of intracranial pathology: preliminary observations and comparisons to 3T and 1.5T. *Neuroimage*. 2018;168:459-476.
15. Ugurbil K. Magnetic resonance imaging at ultrahigh fields. *IEEE Trans Biomed Eng*. 2014;61:1364-1379.
16. Keil B, Wald LL. Massively parallel MRI detector arrays. *J Magn Reson*. 2013;229:75-89.
17. Vaidya MV, Sodickson DK, Lattanzi R. Approaching ultimate intrinsic SNR in a uniform spherical sample with finite arrays of loop coils. *Concepts Magn Reson Part B Magn Reson Eng*. 2014;44:53-65.
18. Lakshmanan K, Cloos M, Brown R, Lattanzi R, Sodickson DK, Wiggins GC. The "Loopole" antenna: a hybrid coil combining loop and electric dipole properties for ultra-high-field MRI. *Concepts Magn Reson Part B Magn Reson Eng*. 2020;2020:1-9.
19. Yan X, Gore JC, Grissom WA. Self-decoupled radiofrequency coils for magnetic resonance imaging. *Nat Commun*. 2018;9:3481.
20. Yan X, Gore JC, Grissom WA. Traveling-wave meets standing-wave: a simulation study using pair-of-transverse-dipole-ring (PTDR) coils for adjustable longitudinal coverage in ultra-high field MRI. *Concepts Magn Reson Part B Magn Reson Eng*. 2018;48B(4):e21402. doi:10.1002/cmr.b.21402
21. Raaijmakers AJ, Ipek O, Klomp DW, et al. Design of a radiative surface coil array element at 7 T: the single-side adapted dipole antenna. *Magn Reson Med*. 2011;66:1488-1497.
22. Woo MK, DelaBarre L, Waks MT, et al. Evaluation of 8-channel radiative antenna arrays for human head imaging at 10.5 tesla. *Sensors (Basel)*. 2021;21(18):6000. doi:10.3390/s21186000
23. Adriany G, Van de Moortele PF, Ritter J, et al. A geometrically adjustable 16-channel transmit/receive transmission line array for improved RF efficiency and parallel imaging performance at 7 tesla. *Magn Reson Med*. 2008;59:590-597.
24. Grier MD, Yacoub E, Adriany G, et al. Ultra-high field (10.5T) diffusion-weighted MRI of the macaque brain. *Neuroimage*. 2022;255:119200.
25. He X, Erturk MA, Grant A, et al. First in-vivo human imaging at 10.5T: imaging the body at 447 MHz. *Magn Reson Med*. 2020;84:289-303.
26. Le Ster C, Grant A, Van de Moortele PF, et al. Magnetic field strength dependent SNR gain at the center of a spherical phantom and up to 11.7T. *Magn Reson Med*. 2022;88:2131-2138.
27. Ugurbil K, Van de Moortele PF, Grant A, et al. Progress in imaging the human torso at the ultrahigh fields of 7 and 10.5 T. *Magn Reson Imaging Clin N Am*. 2021;29:e1-e19.
28. Yacoub E, Grier MD, Auerbach EJ, et al. Ultra-high field (10.5 T) resting state fMRI in the macaque. *Neuroimage*. 2020;223:117349.
29. Sadeghi-Tarakameh A, Jungst S, Lanagan M, et al. A nine-channel transmit/receive array for spine imaging at 10.5 T: Introduction to a nonuniform dielectric substrate antenna. *Magn Reson Med*. 2022;87:2074-2088.
30. Sadeghi-Tarakameh A, DelaBarre L, Lagore RL, et al. In vivo human head MRI at 10.5T: a radiofrequency safety study and preliminary imaging results. *Magn Reson Med*. 2020;84: 484-496.
31. Lattanzi R, Sodickson DK. Ideal current patterns yielding optimal signal-to-noise ratio and specific absorption rate in magnetic resonance imaging: computational methods and physical insights. *Magn Reson Med*. 2012;68:286-304.
32. Giannakopoulos II, Guryev GD, Serralles JEC, et al. Compression of volume-surface integral equation matrices via Tucker decomposition for magnetic resonance applications. *IEEE Trans Antennas Propag*. 2022;70:459-471.
33. Christ A, Kainz W, Hahn EG, et al. The virtual family—development of surface-based anatomical models of two adults and two children for dosimetric simulations. *Phys Med Biol*. 2010;55:N23-N38.
34. Roemer PB, Edelstein WA, Hayes CE, Souza SP, Mueller OM. The NMR phased array. *Magn Reson Med*. 1990;16:192-225.
35. Lattanzi R, Grant AK, Polimeni JR, et al. Performance evaluation of a 32-element head array with respect to the ultimate intrinsic SNR. *NMR Biomed*. 2010;23:142-151.
36. Pruessmann KP, Weiger M, Scheidegger MB, Boesiger P. SENSE: sensitivity encoding for fast MRI. *Magn Reson Med*. 1999;42:952-962.
37. Montin E, Wiggins R, Block KT, Lattanzi R. MR optimum – a web-based application for signal-to-noise ratio evaluation. Proc Int Soc. *Magn Reson Med*. 2019;27:4617.
38. Georgakis I, Giannakopoulos I, Mikhail S, Athanasios G. A fast volume integral equation solver with linear basis functions for the accurate computation of electromagnetic fields in MRI. *IEEE Trans Antennas Propag*. 2020;69:13.
39. Polimeridis AG, Villena JF, Daniel L, White JK. Stable FFT-JVIE solvers for fast analysis of highly inhomogeneous dielectric objects. *J Comput Phys*. 2014;269:280-296.
40. Georgakis IP, Villena JF, Polimeridis AG, Lattanzi R. Novel numerical basis sets for electromagnetic field expansion in arbitrary inhomogeneous objects. *IEEE Trans Antennas Propag*. 2022;70:8227-8241.
41. Lattanzi R, Wiggins GC, Zhang B, Duan Q, Brown R, Sodickson DK. Approaching ultimate intrinsic signal-to-noise ratio with loop and dipole antennas. *Magn Reson Med*. 2018;79:1789-1803.
42. Adriany G, Radder J, Tavaf N, et al. *Evaluation of a 16-Channel Transmitter for Head Imaging at 10.5T*. IEEE; 2019 2019/9/12:1171-1174.
43. Terman F. *Radioengineer's Handbook*. Mc Graw Hill; 1943.
44. Waks M, Tavaf N, Lagore R, et al. Ugurbil K. A 16- channel splitable non-overlapped self-decoupled loop transmitter for 10.5 tesla human head imaging. *Proc Int Soc Mag Reson Med*. 2022;4109.
45. Waks M, Lagore RL, Auerbach E, et al. A self-decoupled 16-channel transmit, 80-channel receive array for 10.5 tesla human head imaging. *Proc Int Soc Mag Reson Med*. 2023;211.
46. Ugurbil K, Auerbach E, Moeller S, et al. Brain imaging with improved acceleration and SNR at 7 tesla obtained with 64-channel receive array. *Magn Reson Med*. 2019;82:495-509.
47. Zaretskaya N. Zooming-in on higher-level vision: high-resolution fMRI for understanding visual perception and awareness. *Prog Neurobiol*. 2021;207:101998.
48. Hoult DI, Phil D. Sensitivity and power deposition in a high-field imaging experiment. *J Magn Reson Imaging*. 2000;12:46-67.
49. Lawrence SJD, Formisano E, Muckli L, de Lange FP. Laminar fMRI: applications for cognitive neuroscience. *Neuroimage*. 2019;197:785-791.
50. Norris DG, Polimeni JR. Laminar (f)MRI: a short history and future prospects. *Neuroimage*. 2019;197:643-649.
51. Weldon KB, Olman CA. Forging a path to mesoscopic imaging success with ultra-high field functional magnetic resonance imaging. *Philos Trans R Soc Lond B Biol Sci*. 1815;2021:20200040.

15222594, 2024, 3, Downloaded from https://onlinelibrary.wiley.com/doi/10.1002/mrm.30108, Wiley Online Library on [01/08/2024]. See the Terms and Conditions (https://onlinelibrary.wiley.com/terms-and-conditions) on Wiley Online Library for rules of use; OA articles are governed by the applicable Creative Commons License

52. Ugurbil K. What is feasible with imaging human brain function and connectivity using functional magnetic resonance imaging. *Philos Trans R Soc Lond B Biol Sci*. 2016;371:20150361.
53. Finn ES, Huber L, Bandettini PA. Higher and deeper: bringing layer fMRI to association cortex. *Prog Neurobiol*. 2021;207:101930.
54. Self MW, van Kerkoerle T, Goebel R, Roelfsema PR. Benchmarking laminar fMRI: neuronal spiking and synaptic activity during top-down and bottom-up processing in the different layers of cortex. *Neuroimage*. 2019;197:806-817.
55. Poplawsky AJ, Fukuda M, Kim SG. Foundations of layer-specific fMRI and investigations of neurophysiological activity in the laminarized neocortex and olfactory bulb of animal models. *Neuroimage*. 2019;199:718-729.
56. Jorgenson LA, Newsome WT, Anderson DJ, et al. The BRAIN initiative: developing technology to catalyse neuroscience discovery. *Philos Trans R Soc Lond B Biol Sci*. 2015;370:20140164.
57. BRAIN Initiave 2.0: From Cells to Circuits, Toward Cures (BRAIN 2.0). 2019.
58. Grant A, Metzger GJ, Van de Moortele PF, et al. 10.5 T MRI static field effects on human cognitive, vestibular, and physiological function. *Magn Reson Imaging*. 2020;73:163-176.
59. Yang QX, Wang J, Zhang X, et al. Analysis of wave behavior in lossy dielectric samples at high field. *Magn Reson Med*. 2002;47:982-989.
60. Van de Moortele PF, Akgun C, Adriany G, et al. B(1) destructive interferences and spatial phase patterns at 7 T with a head transceiver array coil. *Magn Reson Med*. 2005;54:1503-1518.
61. Tavaf N, Lagore RL, Jungst S, et al. A self-decoupled 32-channel receive array for human-brain MRI at 10.5 T. *Magn Reson Med*. 2021;86:1759-1772.
62. Tavaf N, Jungst S, Lagore R, et al. A Self-decoupled 64 channel receive Array for human brain MRI at 10.5T. *Proc Int Soc Magn Reson Med*. 2021;29:179.
63. Wiesinger F, Van de Moortele PF, Adriany G, De Zanche N, Ugurbil K, Pruessmann KP. Parallel imaging performance as a function of field strength—an experimental investigation using electrodynamic scaling. *Magn Reson Med*. 2004;52:953-964.
64. Wiesinger F, Van de Moortele PF, Adriany G, De Zanche N, Ugurbil K, Pruessmann KP. Potential and feasibility of parallel MRI at high field. *NMR Biomed*. 2006;19:368-378.
65. Gruber B, Stockmann JP, Mareyam A, et al. A 128-channel receive array for cortical brain imaging at 7 T. *Magn Reson Med*. 2023;90:2592-2607.
66. Wiggins GC, Polimeni JR, Potthast A, Schmitt M, Alagappan V, Wald LL. 96-channel receive-only head coil for 3 tesla: design optimization and evaluation. *Magn Reson Med*. 2009;62:754-762.
67. Avdievich NI, Nikulin AV, Ruhm L, et al. A 32-element loop/dipole hybrid array for human head imaging at 7 T. *Magn Reson Med*. 2022;88:1912-1926.
68. Sadeghi-Tarakameh A, Waks M, Grant A, et al. Boosting central head SNR at 10.5T: 32-channel hybrid RF coil comprised of 25 Rx-only loops and 7 TxRx NODES dipoles. *Proc Int Soc Mag Reson Med*. 2023;3913.
69. Lagore RL, Grant A, DelaBarre L, et al. 128-channel brain imaging array with improved acceleration at 10.5 tesla. *Proc Int Soc Mag Reson Med*. 2023;1059.
70. Vizioli L, Moeller S, Dowdle L, et al. Lowering the thermal noise barrier in functional brain mapping with magnetic resonance imaging. *Nat Commun*. 2021;12:5181.
71. Uludag K, Muller-Bierl B, Ugurbil K. An integrative model for neuronal activity-induced signal changes for gradient and spin echo functional imaging. *Neuroimage*. 2009;48:150-165.
72. Uludag K, Ugurbil K. Physiology and physics of the fMRI signal. In: Uludag K, Ugurbil K, Berliner L, eds. *fMRI: from Nuclear Spins to Brain Function, Biological Magnetic Resonance*. Springer; 2015:163-214.
73. Ogawa S, Menon RS, Tank DW, et al. Functional brain mapping by blood oxygenation level-dependent contrast magnetic resonance imaging. A comparison of signal characteristics with a biophysical model. *Biophys J*. 1993;64:803-812.

How to cite this article: Zhang B, Radder J, Giannakopoulos I, et al. Performance of receive head arrays versus ultimate intrinsic SNR at 7 T and 10.5 T. *Magn Reson Med*. 2024;92:1219-1231. doi: 10.1002/mrm.30108

15222594, 2024, 3, Downloaded from https://onlinelibrary.wiley.com/doi/10.1002/mrm.30108, Wiley Online Library on [01/08/2024]. See the Terms and Conditions (https://onlinelibrary.wiley.com/terms-and-conditions) on Wiley Online Library for rules of use; OA articles are governed by the applicable Creative Commons License